Materials Advances

ROYAL SOCIETY OF CHEMISTRY

PAPER

View Article Online
View Journal | View Issue

Cite this: *Mater. Adv.*, 2026, 7, 1552

Amplified photocatalytic performance of UiO-66-NH_2/BiOI@α-Bi_2O_3 ternary heterojunctions towards Congo red degradation and H_2O_2 production

Anubhav Naik,[a] Kundan Kumar Das,[b] Prakash Chandra Sahoo[a] and Rashmi Acharya *[a]

Designing an efficient photocatalytic system that achieves a broad visible-light absorption window and a minimal recombination rate has been challenging. In this work, we have depicted UiO-66-NH_2/BiOI@α-Bi_2O_3 ternary heterostructures' (BBUN) fabrication *via* a simple solvothermal approach. FESEM and TEM studies revealed that BBUN-4 consists of UiO-66-NH_2 (UN) nanoparticles, BiOI microspheres (BM), and *in situ* derived α-Bi_2O_3 nanorods (BR). The morphology of BM and BR was manipulated by varying the BM and *N*,*N*-dimethylformamide (DMF) ratio. It was observed that BM microspheres and BR nanorods were obtained when the BM : DMF ratio was maintained at 7.5 : 1. Besides, the interaction of DMF incorporated abundant oxygen vacancies (O_v) in BM and BR. The introduction of abundant oxygen vacancies (O_v) markedly broadened the light absorption edge up to 665 nm. The existence of an O_v–Bi–N interfacial charge transport channel momentously improved the charge transfer and separation rate, as evidenced from PL, EIS, and LSV studies. XPS results, Mott–Schottky analysis, and scavenging tests collectively corroborated the formation of a double Z-scheme BBUN heterojunction. The photocatalytic CR degradation rate for BBUN-4 was determined to be 3.05 and 3.43 times greater than that of pristine UN and BM, respectively. BBUN-4 exhibited H_2O_2 production of 322 μmol L^{-1}, whereas that obtained over BM and UN was only 127 and 164 μmol L^{-1}, respectively.

Received 16th October 2025,
Accepted 15th December 2025

DOI: 10.1039/d5ma01197c

rsc.li/materials-advances

1. Introduction

Growing energy demand, gradual depletion of conventional energy fuels, and alarmingly rising environmental issues have led researchers to develop sustainable technologies. Semiconductor-mediated photocatalysis is an environmentally benign avenue that uses inexhaustible sunlight and earth-abundant water for the successful addressing of these challenges.[1–3] Nevertheless, inadequate availability of charge carriers, narrow light absorption window, a faster rate of electron–hole pair recombination, low surface area, and weaker redox abilities are some of the inherent features of semiconductor photocatalysts that hinder their practical applications. Designing porous nanostructures with varying dimensionality, selecting suitable semiconductor photocatalysts, creating atomic defects, constructing Z-scheme charge dynamics, and establishing charge transport channels are the crucial aspects to overcome these bottlenecks.

Amongst the wide range of investigated semiconductors, metal–organic frameworks (MOFs) have attracted stupendous attention in diversified photocatalytic applications for their intrinsic characteristics, like tunable porous architecture, high surface area, crystalline structure, and stability.[4–6] Recently, UiO-66-NH_2 nanoparticles have been recognised as a versatile photocatalyst due to their enhanced aqueous stability and their enlarged surface area and porous structure.[7] Moreover, the lone pair of electrons on the N atom of NH_2 groups can interact with the π*-antibonding orbitals of benzene rings and experience a bathochromic shift in visible light absorption.[8] However, it still suffers from a high rate of charge carrier recombination and poor visible light response. Constructing heterojunctions with one or more visible light-responsive semiconductors having preferred band potentials is a promising strategy to hinder the recombination of charge carriers and widen the visible light absorption window.[9] BiOI with a small band gap energy (E_g = 1.77–1.92 eV) enables robust photo response in the visible region. Its large positive valence band potential accelerates the water oxidation reaction to generate hydroxyl ions (•OH),

[a] *Department of Chemistry, I.T.E.R, Siksha 'O' Anusandhan Deemed to be University, Bhubaneswar, Odisha-751030, India.*
E-mail: drrashmiacharya75@gmail.com, rashmiacharya@soa.ac.in;
Fax: +91-674-2350642; Tel: +91-674-2351777
[b] *Centre for Nano Science and Nano Technology, ITER, Siksha 'O' Anusandhan Deemed to be University, Bhubaneswar, Odisha-751030, India*

which aids in pollutant degradation.[10] Ji *et al.* fabricated a BiOI nanosheet-anchored UiO-66-NH_2 direct Z-scheme heterojunction, which exhibited a faster bisphenol A photodegradation rate as compared to the pristine counterparts.[11] However, double Z-scheme heterojunctions constitute a sophisticated class of photocatalytic materials engineered to substantially improve photocatalytic efficiency. In this configuration, three semiconductors are strategically combined to establish two consecutive Z-scheme charge-transfer routes. Electrons generated in the oxidation component are first neutralized by holes in the middle semiconductor, and then another similar recombination happens at the second interface. Through this electron–hole neutralization, only the low-energy carriers are eliminated, while the electrons possessing the highest reduction power and the holes exhibiting the strongest oxidative potential remain spatially isolated. This unique charge-flow pattern effectively minimizes bulk recombination, ensures long-lived carrier separation, and strengthens the intrinsic redox capability, enabling efficient execution of divergent photocatalytic reactions such as water splitting, H_2O_2 synthesis, advanced pollutant mineralization *etc.*[12]

α-Bi_2O_3 with excellent oxidation properties possesses an appropriate band gap energy (2.5–2.8 eV) for visible light absorption and can be applied for visible light photocatalysis.[13] Moreover, it can be derived from BiOI, with the simultaneous formation of BiOI@α-Bi_2O_3. *In situ* synthesis of BiOI@α-Bi_2O_3 not only accumulates the features of both but also makes the process cost-effective. Yan *et al.* constructed an Ag–AgI/BiOI–Bi_2O_3 dual Z-scheme heterojunction containing an assembly of BiOI nanosheets, Bi_2O_3 flakes, and AgI nanoparticles by synthesising BiOI@Bi_2O_3 *in situ*. They reported that the heterojunction exhibited enhanced photoactivity due to the optimised redox ability, faster charge separation rate, and larger specific surface area. About 95% of the methyl orange was degraded by the heterojunction photocatalyst when exposed to visible light.[14] Designing 3D porous BiOI spheres accelerates light harvesting ability through multiple reflections, thereby enriching photoinduced excitons. On the other hand, the fabrication of α-Bi_2O_3 nanorods can inhibit the recombination rate by demonstrating unidirectional migration of excitons and a short surface charge transfer distance.[15] Although Zhang *et al.* reported the spherical morphology of BiOI in the *in situ* prepared BiOI@Bi_2O_3 based double Z-scheme heterojunction through the solvothermal technique, Bi_2O_3 nanorods were not formed.[16] Solvothermal temperature, nature of solvents, solvent to solid ratio, *etc.*, are considered vital to obtain heterojunctions of desired topology for ameliorated photocatalytic performance.

Congo red (CR), an anionic diazo dye, finds extensive applications in the textile, printing, and paper industries. It is highly soluble in water and hard to degrade, making it a persistent pollutant in aquatic ecosystems.[17] When discharged into water bodies without adequate treatment, it poses multiple environmental and health risks. Due to its bright colour, CR in water bodies severely affects the aesthetic quality of the environment and blocks sunlight penetration, disrupting the photosynthesis process in aquatic plants. This, in turn, reduces the oxygen level in the water, leading to the death of fish and other aquatic life. Direct exposure to CR or its derivatives can cause skin irritation and respiratory issues, and potentially long-term exposure could lead to cancer.[18] The persistence and detrimental effects of CR pose an urgent need for its sustainable degradation into harmless products. Although several studies have reported its photocatalytic destruction, investigations of high CR concentrations with minimal catalytic doses have rarely been reported.

Hydrogen peroxide (H_2O_2) is an important chemical widely used in energy conversion, chemical synthesis, and environmental remediation.[19] The application of conventional synthesis approaches like the electrochemical technique, the anthraquinone method, and the oxidation of alcohol for its manufacture is restricted due to high cost, stringent environmental regulations, and significant energy consumption. In contrast, photocatalytic H_2O_2 production through two-electron dioxygen reduction has emerged as an environmentally benevolent and energy-inexpensive approach.[20,21] In the context of the lethality of CR in the environment and the importance of H_2O_2 production in mitigating the energy crisis as well as curbing environmental pollution, it is indispensable to develop a cost-effective and viable photocatalytic system.

Herein, we have explored the fabrication of UiO-66-NH_2/BiOI@α-Bi_2O_3 ternary heterojunction photocatalysts through a two-step solvothermal approach. At first, BM microspheres were synthesised by treating a mixture of $Bi(NO_3)_3$ and KI in ethylene glycol at 150 °C for 12 hours. In the second step, BM microspheres of a known amount were treated with a mixture of $ZrCl_4$, 2-amino terephthalic acid (2-ATP), and DMF at 120 °C for 24 hours in a Teflon-lined autoclave to obtain the desired products. FESEM and TEM images demonstrated that the integration of UN nanoparticles, BM microspheres, and *in situ* produced BR nanorods resulted in the successful formation of a ternary BBUN heterojunction. The elevated temperature and pressure prevailed in the reactor, followed by the interaction of DMF and 2-ATP with the BM, resulting in its partial decomposition into α-Bi_2O_3 nanorods. The morphologies of BM and BR in the heterostructure were controlled by the weight-to-volume ratio between BM and DMF. The interaction of DMF with BM and BR also promoted the incorporation of O_v, which extended the light absorption towards the red end of the visible region, as confirmed by UV-Vis-DRS spectra. The anchoring of UiO-66-NH_2 nanoparticles through the coordination of NH_2 groups with Bi^{3+} of the BM microspheres and BR nanorods resulted in the emergence of Bi–N interfacial bonds, thereby establishing the O_v–Bi–N interfacial charge transport channels. Based on the results obtained from XPS studies, band potential measurements, and radical scavenging tests, a double Z-scheme charge transfer mechanism has been suggested. The heterostructure prepared with 600 mg BM (BBUN-4) demonstrated superior photocatalytic activity for the remediation of CR from aqueous solution and H_2O_2 production. This enhancement is ascribed to the construction of a morphology-controlled ternary heterojunction, O_v in BM and BR, as well as O_v–Bi–N interfacial charge transport channels. The current work explores the possibility of designing morphology-regulated oxygen vacancy-rich binary Z-scheme heterojunctions to achieve superior photocatalytic degradation of organic dyes and H_2O_2 production.

2. Experimental section

Detailed information on the chemicals, synthetic procedures of BR, material characterization techniques, optical and electrochemical measurements, photocatalytic CR degradation efficiency evaluation, and photocatalytic H_2O_2 production is provided in the SI (S1).

2.1 BiOI microsphere synthesis

A solvothermal synthesis approach was followed to fabricate BM, as reported earlier.[22] In a typical synthesis, 1.376 mg of $Bi(NO_3)_3{\cdot}5H_2O$ was solubilised in 40 ml of ethylene glycol (ELG) under continuous stirring for 30 minutes and was labelled as solution A. Solution B was made by dissolving 0.47 mg of KI in 40 ml of ELG under identical conditions. Then B was mixed with A, and the mixture was subjected to stirring for 1 h. After that, the mixture was treated at 150 °C for 12 h in a Teflon-lined autoclave. The orange-coloured mass so formed was washed with double-distilled water repeatedly, followed by washing with ethanol. The resulting mass was heated at 60 °C in a vacuum oven for 12 h to get BM.

2.2 Fabrication of a UiO-66-NH_2/BiOI@α-Bi_2O_3 ternary heterojunction

A simple solvothermal technique was employed to fabricate UiO-66-NH_2/BiOI@α-Bi_2O_3 heterojunctions. 1 mmol $ZrCl_4$ and 1 mmol 2-ATP were dissolved in 40 ml of DMF separately. The two solutions were mixed and subjected to stirring for 30 minutes. Then, a predetermined amount of BM was added to the mixture solution, followed by stirring for another 30 minutes. The mixture solution was treated at 120 °C for 24 h in a Teflon-lined autoclave. The autoclave was then cooled to room temperature, and the product was filtered. The obtained solid was repeatedly rinsed with distilled water and ethanol, followed by drying overnight at 80 °C to obtain the desired product. The fabricated photocatalysts were named as BBUN-1, BBUN-2, BBUN-3, BBUN-4, and BBUN-5, depending on the weight of BM as 50 mg, 200 mg, 400 mg, 600 mg, and 800 mg, respectively. The synthesis procedure of the BBUN heterostructure was presented in Scheme 1. A similar procedure was followed to synthesize pristine UN, without the addition of BM.

3. Results and discussion

3.1 Morphology and microstructure

The surface morphology of the synthesised samples was analysed using FESEM. The FESEM images of UN, BM, and BBUN-4 are displayed in Fig. 1. As observed in Fig. 1(a), the fine nanoparticles of UN were joined together to form a sphere-like morphology with a rough surface containing a large number of voids. Such architectures suggested that the UN may possess a high specific surface area with numerous surface-active sites, which are advantageous for the efficient adsorption of reacting species on its

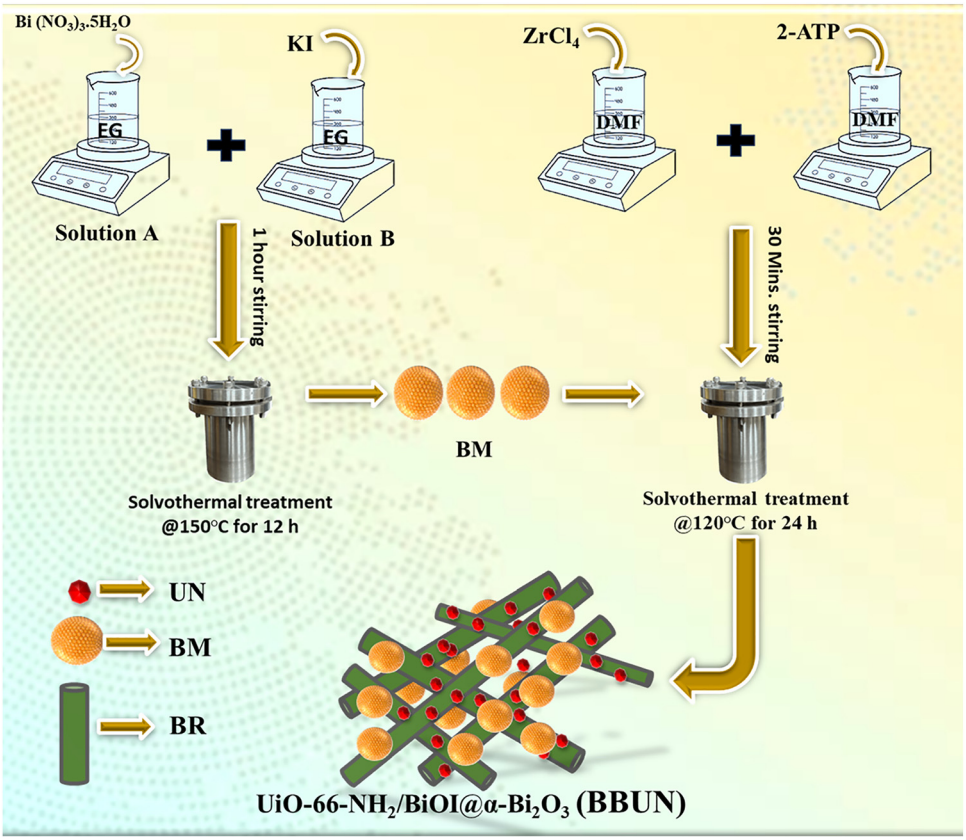

Scheme 1 Schematic illustration for the fabrication of UiO-66-NH_2/BiOI@α-Bi_2O_3 (BBUN) ternary heterojunctions.

surface.[23] In Fig. 1(b), BM showed distinct spherical microflowers with particle sizes ranging from 2.5 to 3.8 μm. As shown in the figure, the BM microspheres possessed a porous morphology. In order to validate the formation of the porous structure of the BM microspheres, its enlarged FESEM image is presented in Fig. 1(c). It was revealed from the figure that the two-dimensional (2D) BM sheets were systematically aligned to result in microspheres with interconnected pores. The 3D morphology with an interconnected porous structure is beneficial for increasing the surface area and promoting the charge carriers' concentration by enhancing visible light absorption efficiency through multiple reflections across the porous channel. Moreover, the interconnected pores can hinder the recombination rate by reducing the charge and mass transfer distance.[24] The FESEM image of the BBUN-4 ternary heterojunction is displayed in Fig. 1(d). As observed from the figure, the UN nanoparticles were anchored on the microspheres and nanorods. The appearance of the microsphere confirmed the retention of the 3D morphology with an interconnected porous structure of BM in the composite. However, elevated temperature and high pressure prevailed during the solvothermal treatment, which accelerated the frequency of collisions among the BM microspheres, causing their partial conversion into nanosheets. The electron-donating groups present in the DMF and NH_2 groups of 2-ATP present in the reaction medium interact with Bi^{3+} of the BM nanosheets, while I atoms of BM extend interaction with Zr^{4+} of the UNH precursor. This leads to the gradual weakening of the Bi–I bonds and their subsequent rupture. As a result, there occurs a rearrangement of Bi–O bonds to form α-Bi_2O_3. The bulky methyl groups of DMF impart steric hindrance, which restricts isotropic growth and directs α-Bi_2O_3 to grow in one dimension to obtain nanorods (BR). Further raising the BM/DMF ratio to 10 : 1 in BBUN-5, the smaller number of methyl groups of DMF could not control Bi_2O_3 growth properly. As a result, Bi_2O_3 nanoflakes were obtained, as observed in Fig. S1. It was also observed from the figure that the 3D morphology was completely destroyed with the formation of BM nanosheets owing to the vigorous collision among a large amount of BM microspheres.

The interaction of electron-donating groups of DMF with Bi^{3+} of BM microspheres and BR nanorods also affects the Bi–O bonds, resulting in the introduction of oxygen vacancies (O_v).[25] Incorporated O_{vs} promotes the coordination of NH_2 groups of UN with Bi^{3+}. This facilitates anchoring of UN nanoparticles on the BM microspheres and BR nanorods to form a ternary heterojunction. As shown in the figure, the integration of UN nanoparticles with BR nanorods and BM microspheres resulted in the formation of a BBUN-4 ternary heterojunction along with the existence of numerous voids. All these features amplified the photocatalytic performance of the heterostructure. Fig. 1(e) displays the results of the energy dispersive X-ray spectroscopy (EDS) analysis, and corresponding elemental mapping images presented in Fig. 1(f)–(l) confirm the homogenous distribution of C, Bi, N, O, I, and Zr elements on the surface of the synthesised heterojunction. The existence of carbon (C) might be attributed to the presence of 2-ATP in BBUN-4 and the carbon tapes used in the FESEM analysis.

A transmission electron microscope (TEM) image of BBUN-4 is shown in Fig. 2(a). It was revealed from the figure that BR possessed a rod-shaped structure with an average length and width of 1.2 μm and 0.27 μm, respectively. Octahedral UN nanoparticles, BM microspheres, and BR nanorods are interconnected thoroughly to obtain BBUN-4 ternary heterojunctions. Three distinct phases of BBUN-4 have appeared in the HRTEM image [Fig. 2(b)]. The lattice fringe of 0.27 nm corresponds to the (102) plane of BM, while the (−012) plane of BR is characterised

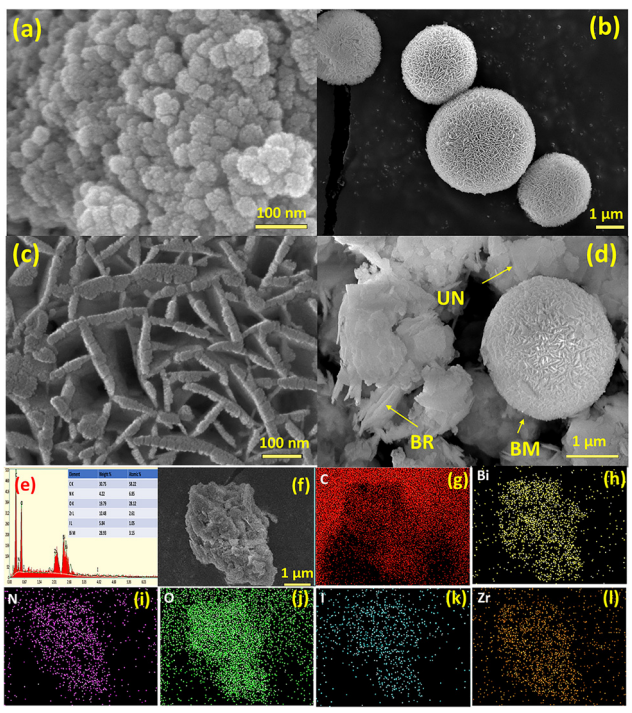

Fig. 1 Field emission scanning electron microscopy (FESEM) images of (a) UN and (b) BM, (c) enlarged FESEM image of BM, (d) FESEM image of BBUN-4, (e) energy dispersive X-ray (EDS) spectrum, (f) elemental mapping images of BBUN-4, (g) C, (h) Bi, (i) N, (j) O, (k) I, and (l) Zr.

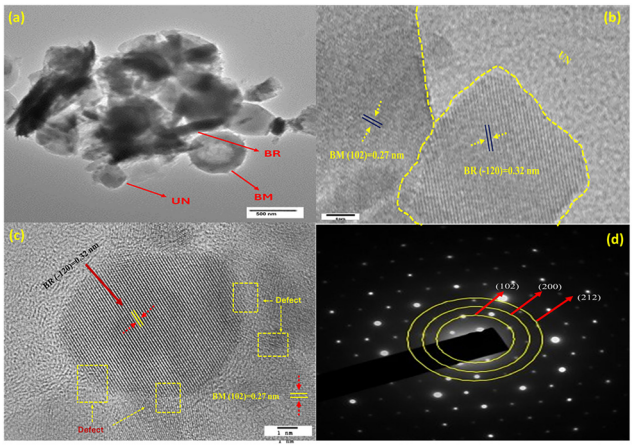

Fig. 2 (a) Transmission electron microscopy (TEM) image, (b) and (c) high-resolution TEM (HRTEM) images, and (d) selected area electron diffraction (SAED) pattern of the BBUN-4 heterostructure.

by the lattice spacing of 0.32 nm.[26,27] The region with no lattice fringe indicates the UN phase. These results demonstrated that the successful integration of UN with BM and BR during the solvothermal treatment constructed a robust BBUN-4 ternary heterojunction, which is consistent with the observations made in FESEM analysis. Furthermore, Fig. 2(c) illustrates that the defects that appeared in the lattice fringes of BM and BR of the heterostructure may be attributed to the oxygen-rich vacancies incorporated at the interfaces. The selected area electron diffraction (SAED) pattern shown in Fig. 2(d) exhibited polycrystalline rings, reflecting a well-defined crystalline structure and confirming the polycrystalline characteristics of the synthesised BBUN-4 heterojunction.[28]

The N_2 adsorption–desorption technique was employed to evaluate the specific surface area and pore volume of BM, UN, and BBUN-4. As shown in Fig. 3(a)–(c), the adsorption isotherms of BM, UN, and BBUN-4 revealed type IV isotherms, with a characteristic H3 hysteresis loop indicating the presence of a mesoporous structure.[29] The BET surface area and pore volumes of BM, UN, and BBUN-4 are presented in Fig. 3(d) and (e), respectively. Pristine UN exhibited a relatively larger surface area of 502.3 $m^2\ g^{-1}$, which can be attributed to its rough and porous morphology, as evident from the FESEM image. Similarly, the 3D morphology with an interconnected porous structure revealed from FESEM studies contributed to the high surface area of 86.3 $m^2\ g^{-1}$ for bare BM. The integration of UN, BM, and *in situ* produced BR enhanced the surface area of BBUN-4 to 525.97 $m^2\ g^{-1}$. It was observed from Fig. 3(e) that the pore volume of BBUN-4 was higher than that of its pristine counterparts. The enhanced surface area and pore volume of the ternary composite are responsible for possessing numerous active surface sites, which are advantageous for increased CR adsorption and O_2 activation.

3.2 Crystal structure and chemical states

X-ray diffraction (XRD) analysis was employed to investigate the structural and crystalline properties of the synthesised photocatalysts. Fig. 4(a) displays the XRD patterns of the UN, BR, and BBUN heterostructures. The diffraction peaks at 2θ = 7.3°, 8.4°, and 25.6°, corresponding to the (111), (200), and (442) planes, confirmed the successful synthesis of pristine UN.[30] The characteristic peaks observed at 2θ = 25.7°, 27.3°, 28.0°, 33.0°, 33.2°, 37.6°, and 46.3° can be indexed to the (002), (−120), (012), (121), (200), (112), and (041) planes, respectively, of monoclinic BR (JCPDS no. 14-0699).[31] In the BBUN heterojunctions, the presence of UN is evident from the diffraction peak at 2θ = 7.3°, with decreased intensity. This peak intensity decrease may be ascribed to the reduction in crystallinity due to the formation of the composite.[32] Furthermore, the appearance of peaks at 2θ = 12.2° (001), 33.0° (102), and 57.6° (212) in the composites corresponds to the tetragonal phase of BM, as per JCPDS no. 85-0863. Notably, the presence of peaks at 2θ = 25.7°, 27.3°, 28.0°, 33.2°, and 46.3° evidenced the presence of BR in the heterojunctions. The peaks corresponding to the (002) and (−120) planes of BR displayed a lower angle shift in the synthesized heterostructures, suggesting lattice distortion due to strong interactions among UN, BR, and BM.[33] The sharp and well-defined peaks in the XRD patterns associated with UN, BM, and BR indicate the successful synthesis of BBUN ternary heterojunctions with a high degree of crystallinity.

Fourier transform infrared (FTIR) spectroscopy was employed to characterise the surface functional groups in the

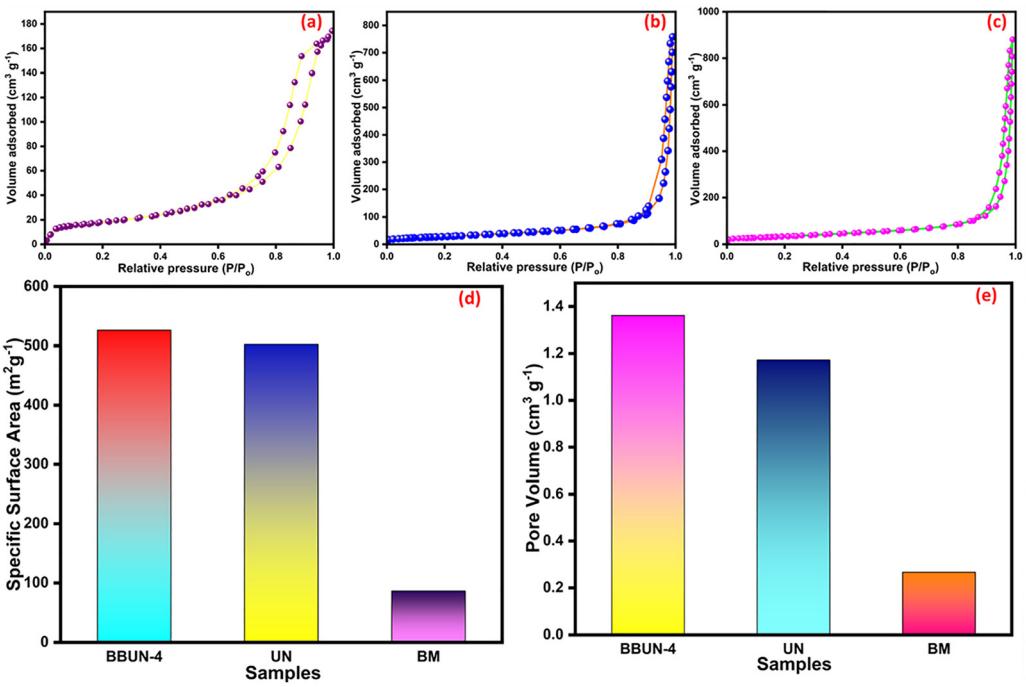

Fig. 3 N_2 sorption isotherms of (a) BM, (b) UN, and (c) BBUN-4, (d) specific surface area, and (e) pore volume of UN, BM, and BBUN-4.

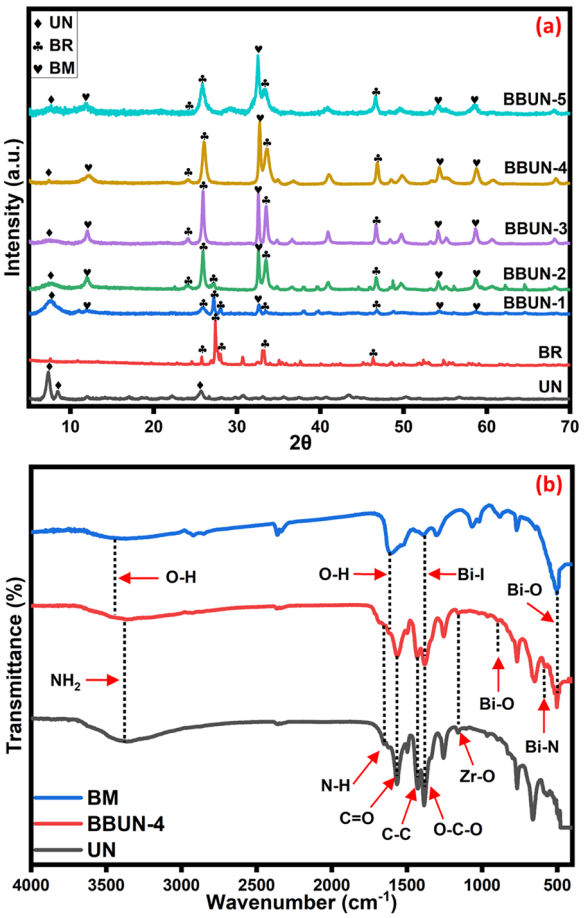

Fig. 4 (a) X-ray diffraction (XRD) patterns of the pristine UN, BR, and BBUN composites, (b) Fourier transform infrared (FTIR) spectra of UN, BM, and BBUN-4, showcasing the characteristic functional groups and bonding interactions present in the samples.

synthesised samples. Fig. 4(b) illustrates the distinctive absorption peaks for UN, BM, and BBUN-4. The FTIR spectrum of pristine UN displayed a characteristic peak at 3364 cm^{-1}, corresponding to the stretching vibration of N–H bonds present in free NH_2 groups. Bands observed at 1651 cm^{-1} and 1565 cm^{-1} were attributed to N–H bending in aromatic amines and asymmetric stretching of carboxylic groups, respectively. Additional peaks at 1427 cm^{-1} and 1385 cm^{-1} were assigned to C–C stretching and O–C–O symmetric vibrations, correspondingly. A weak absorption band at 1105 cm^{-1} was indicative of Zr–O stretching vibrations from Zr-oxo clusters, while the broad peaks in the range of 400–800 cm^{-1} are associated with Zr(–OC) stretching vibrations of UN MOF.[34] In the spectrum of BM, the peak that appeared at 1391 cm^{-1} was assigned to the stretching vibrations of the Bi–I bond, and a distinctive absorption peak of Bi–O stretching vibrations was observed at 503 cm^{-1}. The peaks around 3400 cm^{-1} and 1603 cm^{-1} correspond to O–H vibrational frequencies of adsorbed water molecules.[35] The presence of characteristic peaks of UN and BM in the BBUN-4 spectrum confirms their presence in the composite. Additionally, the peak that appeared at 893 cm^{-1} corresponds to the stretching mode of the Bi–O bond present in Bi_2O_3. Therefore, it was revealed from this evidence that BR was formed *in situ* during the fabrication of BBUN-4.[36] These outcomes corroborated the successful synthesis of the ternary heterojunction, which was also evident from the XRD results. Furthermore, a distinct vibrational band observed at 588 cm^{-1} can be assigned to the formation of the Bi–N bond.[37] The formation of this bond resulted from the interaction between the Bi^{3+} ions of BM and the $–NH_2$ groups of UN. Bi–N bond formation is indicative of the establishment of an efficient interfacial charge-transfer channel between BM and UN.

X-ray photoelectron spectroscopy (XPS) analysis was performed to investigate the elements' chemical composition and valence states in the prepared samples and the charge transfer dynamics in the ternary heterojunction. The survey spectra of the pristine UN, BM, BR, and BBUN-4 heterostructure are shown in Fig. 5(a). It was evident from the full XPS spectra that the ternary composite contains Zr, N, Bi, O, and I elements, as exhibited by its pristine counterparts. The coexistence of these elements in BBUN-4 was corroborated by elemental mapping and EDS results, which validated the formation of a ternary heterojunction. Fig. 5(b) displays the high-resolution Zr 3d XPS spectra of pristine UN and BBUN-4. The peaks at binding energies 181.7 and 184.0 eV were ascribed to Zr $3d_{5/2}$ and Zr $3d_{3/2}$ spin orbitals of Zr^{4+} of UN, respectively.[38] In the BBUN-4 spectrum, similar peaks have appeared with a negative shift of binding energies at 181.0 and 183.8 eV. The N 1s spectrum of UN, shown in Fig. 5(c), displayed a single peak at 398.2 eV, which indicates the presence of the $–NH_2$ group.[39] However, the N 1s peak was deconvoluted into three peaks at 398.1 eV, 400.3, and 403.1 eV in the BBUN-4 spectrum. The peak at 398.1 eV experienced a shift of 0.1 eV to lower binding energy, corresponding to the presence of the $–NH_2$ group, while the peaks at 400.3 and 403.1 eV might be attributed to the interaction between Bi and N.[40] This interaction resulted in the formation of a Bi–N bond between NH_2 of UN and Bi of BM, as well as that of BR. The existence of this interfacial bond was evident from the FTIR results. The Bi–N bond formation facilitated the establishment of charge transfer channels among BM, BR, and UN in the ternary heterojunction. The Bi 4f spectra of BM, BR, and BBUN-4 are presented in Fig. 5(d). The pristine BM exhibited two distinct peaks at 158.1 eV and 162.4 eV, attributed to Bi $4f_{7/2}$ and Bi $4f_{5/2}$ states, respectively, of Bi^{3+} ions.[41] A similar doublet was observed at 157.1 eV and 163.4 eV for BR.[43] In the BBUN-4 heterojunction, the peaks ascribed to each of the Bi 4f microstates were deconvoluted into two different peaks. The peak at 158.1 eV representing the Bi $4f_{7/2}$ state of BM was relocated at 158.7 eV, whereas that for the Bi $4f_{5/2}$ state experienced a shift of 1.6 eV from 162.4 eV. Similarly, the peak corresponding to the Bi $4f_{7/2}$ of BR was moved to a higher binding energy of 158.2 eV after a jump of 1.1 eV, and that of Bi $4f_{5/2}$ was shifted positively by 0.4 eV to 163.8 eV. Fig. 5(e) represents the O 1s spectrum for BM, BR, and BBUN-4. For BM, the O 1s spectrum was deconvoluted into two peaks at 528.9 eV and 530.3 eV due to the presence of a Bi–O bond and surface hydroxyl groups, correspondingly.[42] These two peaks were observed at binding energies of 528.1 eV and

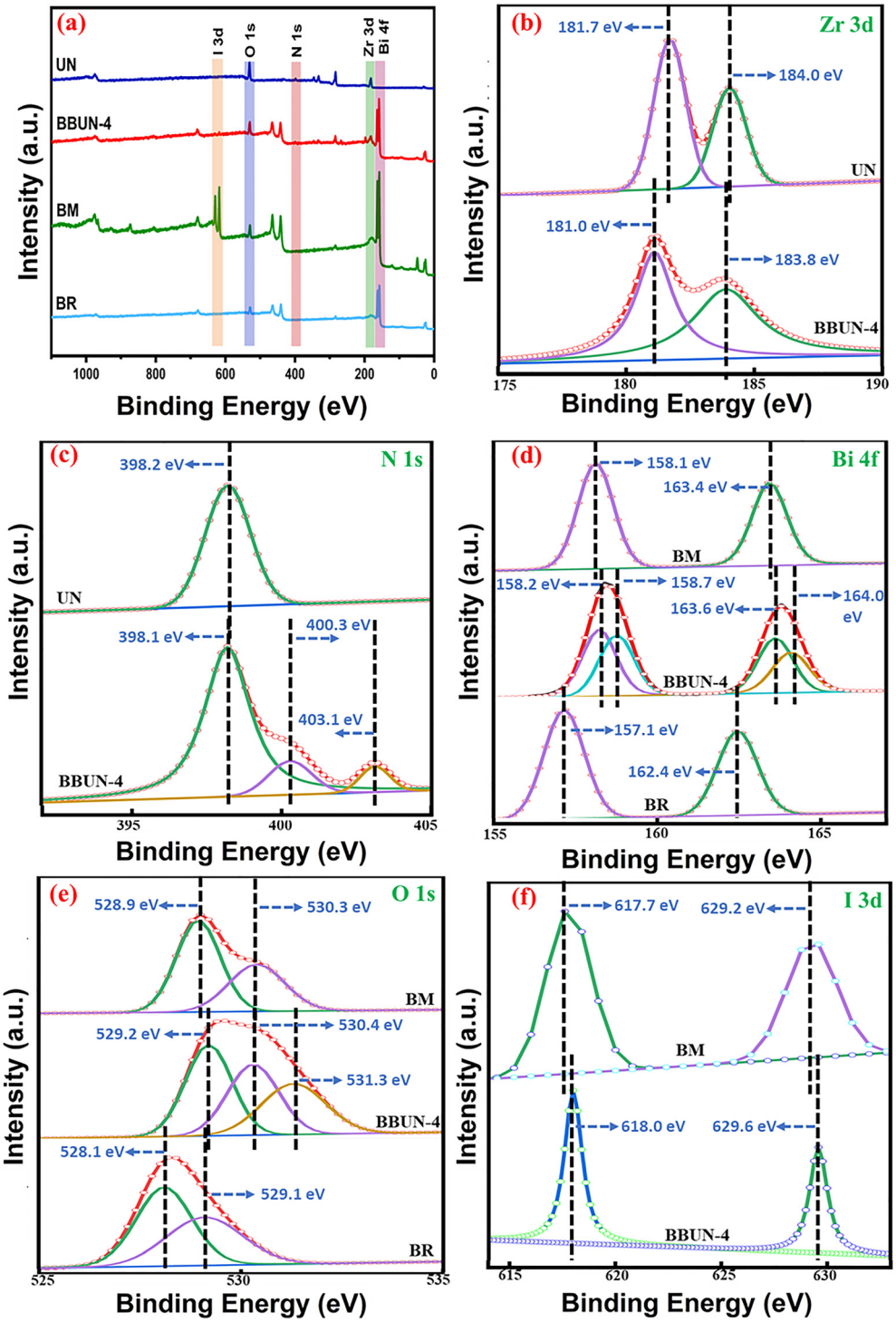

Fig. 5 (a) XPS survey spectra of the BM, BR, UN, and BBUN-4 composites, along with high-resolution XPS spectra of (b) Zr 3d, (c) N 1s, (d) Bi 4f, (e) O 1s, and (f) I 3d.

529.1 eV, respectively, in bare BR.[43] However, the deconvolution of the O 1s spectrum of BBUN-4 resulted in three peaks. The appearance of a peak at 529.2 eV was ascribed to the Bi–O bond, and that at 531.3 eV corresponded to the presence of surface hydroxyl groups. It is worth noting here that these two peaks experienced a positive shift with respect to pristine BM and BR. The third peak at 530.4 eV is attributed to the presence of oxygen-rich vacancies (O_v) formed during the solvothermal synthesis of BBUN-4. This finding, as well as the formation of interfacial defects revealed from HRTEM analysis, validated the formation of O_v at the interfaces of BBUN-4. Incorporating oxygen vacancies can be beneficial for extending the light

absorption range and improving the reactant adsorption ability of BBUN-4.[44] Moreover, these vacancies can trap electrons, thereby preventing the recombination of photogenerated electron–hole pairs.[45] All these features lead the ternary heterojunction to exhibit higher photocatalytic activity. The I 3d spectrum of BM and BBUN-4 was displayed as a characteristic of I^- ions in Fig. 5(f). Two distinct peaks appeared at 617.7 eV and 629.2 eV corresponding to I $3d_{5/2}$ and I $3d_{3/2}$ states, respectively, for BM.[42] In BBUN-4, the peak representing I $3d_{5/2}$ was shifted to a higher binding energy by 0.3 eV, while that appearing at 629.2 eV experienced a positive shift of 0.4 eV. As observed, the negative shift of peaks in the Zr 3d and N 1s spectra of BBUN-4 reflected an increased charge density on UN, which acts as an electron acceptor. On the other hand, the positive shift of peaks in the Bi 4f, O 1s, and I 3d spectra indicated a reduced charge density in BM and BR, making them electron donors. Therefore, XPS studies suggested that photoelectrons can be channelized from BM and BR to UN through the heterojunction formed along the interfacial region of the three semiconductors.

3.3 Optical properties

UV-Vis diffuse reflectance spectroscopy (UV-Vis DRS) was employed to evaluate the optical properties of the synthesised materials over the wavelength range of 200–800 nm. The absorption edges and corresponding band gap energies of the studied semiconductor photocatalysts were determined using this technique. As depicted in Fig. 6(a), the absorption edges of UN and BM were observed at 494 nm and 635 nm, respectively. Interestingly, the DRS spectrum of BBUN-4 displayed a hump in the region of 450 to 530 nm as well as three absorption edges at 473, 538, and 665 nm. The absorption hump in the composite indicated the existence of impurity levels that may be formed by the introduction of O_v in BR and BM.[46] It was reported that the absorption maximum for α-Bi_2O_3 lies around 450 nm, and the corresponding band gap energy is 2.76 eV.[47] The absorption edge observed at 473 nm suggested the presence of α-Bi_2O_3 in BBUN-4 with a bathochromic shift of 23 nm. The spectral band at 665 nm due to BM experienced a 30 nm shift towards the red end of the visible region. This red shift in absorption tail indicated narrowing of the band gaps. As revealed from Fig. 6(b), the band gap energy corresponding to BM in BBUN-4 was decreased from that of its pristine counterpart. The band gap energy corresponding to BR in the composite was found to be lower than that determined in the literature. The lowering of the band gap energy might be attributed to the overlapping of electronic states resulting from the O_{vs} introduced in BR and BM in the ternary composite with the band edges of the semiconductor.[48] The absorption edge corresponding to UN in the composite also experienced a red shift of 44 nm, and the

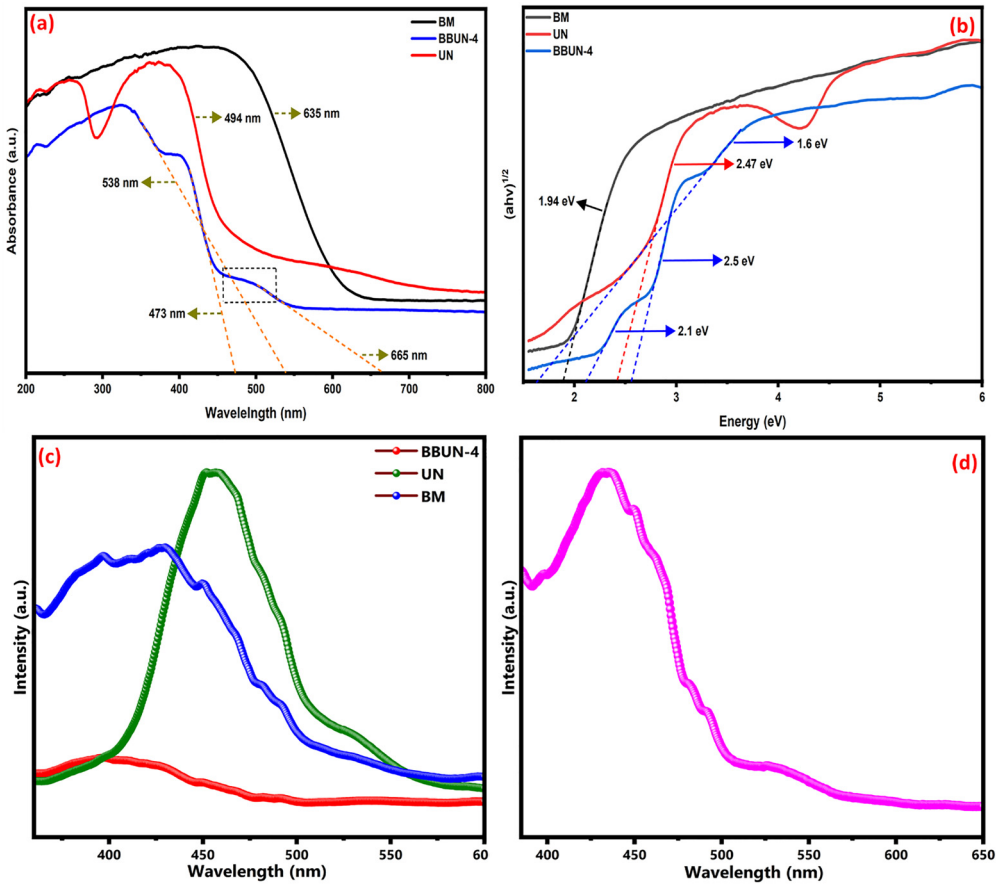

Fig. 6 (a) UV-Vis DRS spectra, (b) Tauc plots of BM, BR, UN, and BBUN-4, and PL spectra of (c) UN, BM an BBUN-4, and (d) BR.

corresponding band gap energy was lower than that of the pristine counterpart. This shift in absorption maximum to longer wavelength and decrease in band gap energy of UN in BBUN-4 might be ascribed to robust interaction of UN with BM and BR, as revealed from FTIR and XPS results. The wide absorption window in the visible region observed for BBUN-4 magnified its ability to harness a large amount of photons from the solar spectrum. Furthermore, the introduction of O_v in BM and BR at the interfaces, overlapping of O_v states with the semiconductor's band edge, and formation of an interfacial Bi–N bond corroborated that there exists an O_v–Bi–N charge transfer channel among BM, BR, and UN at the interface of BBUN-4. The formation of an O_v–Bi–N interfacial charge transfer channel facilitated the separation and migration of photoinduced electron–hole pairs, which in turn suppresses the recombination rate of charge carriers to a considerable extent.

Photoluminescence (PL) emission in photocatalysts arises due to the recombination of photoinduced excitons. A decrease in PL intensity signifies a reduction in charge carriers' recombination rates.[49] The PL spectra of pure UN, BM, and the BBUN-4 composite under 360 nm excitation are shown in Fig. 6(c), while the PL spectrum of BR obtained under 385 nm excitation is presented in Fig. 6(d). The pristine photocatalysts, UN, BR, and BM, exhibited intense PL signals, indicating substantial charge carrier recombination. In contrast, the BBUN-4 composite demonstrated the lowest PL intensity, suggesting a marked reduction in electron–hole recombination rate. The reduced recombination rate may be ascribed to O_v-introduced impurity levels, which act as an electron shuttle to magnify the charge carriers' transfer through the O_v–Bi–N interfacial channel.

3.4 Electrochemical analysis

Electrochemical impedance spectroscopy (EIS) was utilized to investigate the charge transfer resistance of the pristine samples and the BBUN-4 heterojunction. The Nyquist plots obtained from the EIS analysis are illustrated in Fig. 7(a). It was revealed from the figure that BBUN-4 exhibited the smallest impedance in comparison to the pristine counterparts, suggesting its lowest resistance to transferring the charge carriers at the interface.[50] This indicated that the ternary heterojunction has the fastest charge transfer rate or the highest ability for migration of excitons, and hence, has experienced minimal charge recombination rate as revealed from PL studies. The minimum charge transfer resistance offered by BBUN-4 may be ascribed to the existence of the O_v–Bi–N interfacial charge transport channel.

To provide evidence in favour of greater migration of charge carriers in the BBUN-4 heterojunction, linear sweep voltammetry (LSV) was conducted. As illustrated in Fig. 7(b), the LSV analysis demonstrated that UN and BR exhibited minimal anodic current densities of 0.087 mA cm^{-2} and 0.1 mA cm^{-2}, respectively, while BM displayed a low cathodic current density of −0.27 mA cm^{-2}. The low values of current density observed from LSV plots reveal limited charge mobility and minimal charge carrier separation in the pristine samples.[51] Notably, the BBUN-4 heterostructure demonstrated higher cathodic and anodic current responses. At an applied potential of −1.0 V

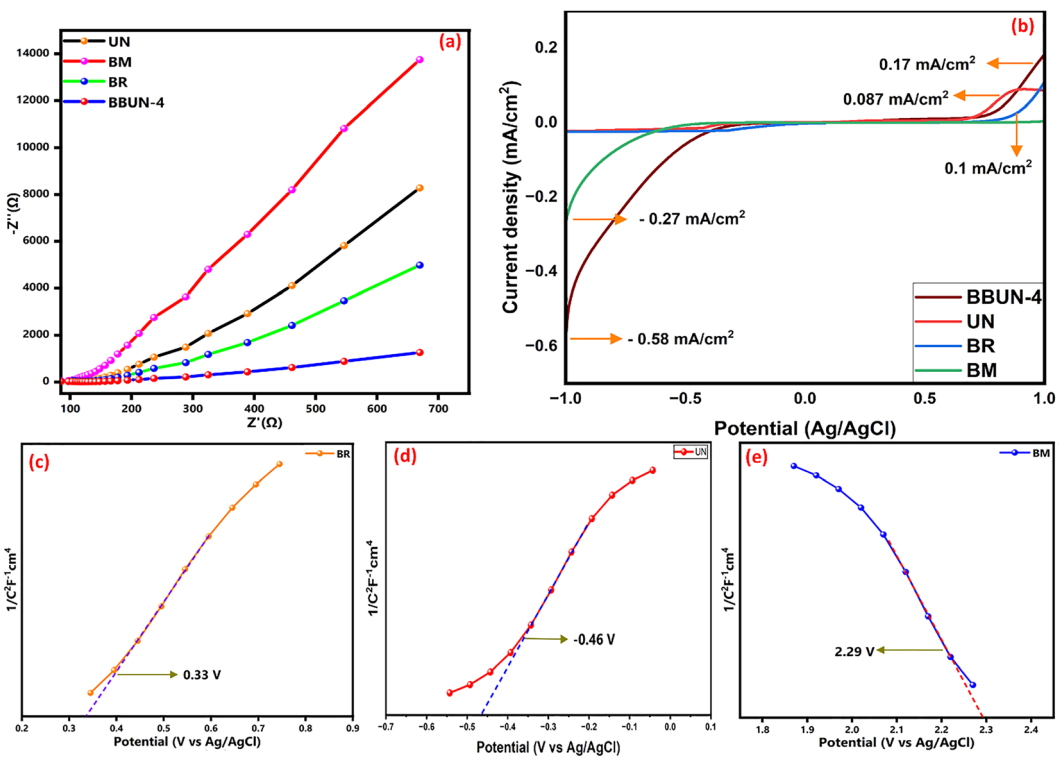

Fig. 7 (a) Electrochemical impedance spectroscopy (EIS), (b) linear sweep voltammetry (LSV) plots of UN, BM, BR, and BBUN-4, and Mott–Schottky plots of (c) BR, (d) UN, and (e) BM.

vs. Ag/AgCl, the cathodic current density reached −0.58 mA cm^{-2}, while the anodic current density of 0.17 mA cm^{-2} was observed at 1.0 V *vs.* Ag/AgCl. The measured photocurrent densities of BBUN-4 were found to be 2.14, 1.95, and 1.7 times more than those obtained for BM, UN, and BR, respectively. The higher current densities shown by BBUN-4 further validated its superior charge transfer ability and enhanced migration ability owing to the existence of O_v–Bi–N interfacial charge transport channels. These results indicate enhanced photogenerated charge carrier migration within the heterojunction. The integration of UN nanoparticles, BM microspheres, and BR nanorods facilitated efficient charge separation and electron transport, resulting in improved photocurrent generation. Furthermore, these findings align with the photoluminescence (PL) studies, which revealed reduced charge recombination, emphasizing the synergistic effect of the morphology-regulated ternary heterostructure and O_v–Bi–N interfacial charge transfer channel in enhancing photocatalytic performance.

Mott–Schottky (MS) analysis was conducted to evaluate BR, UN, and BM's semiconducting characteristics and flat band potentials. As displayed in Fig. 7(c) and (d), the positive slopes in the MS plots of BR and UN revealed their n-type characteristics, whereas the p-type nature of BM was confirmed from the negative slope in its MS plot shown in Fig. 7(e). The flat band potentials, derived from the intercepts of the linear regions in the MS plots, were determined to be 0.33 V, −0.46 V, and 2.29 V (*vs.* Ag/AgCl) for BR, UN, and BM, respectively. These values were further converted to the reversible hydrogen electrode (RHE) scale using eqn (1).[27]

$$E_{RHE} = E_{Ag/AgCl} - 0.0591\ (7 - \text{pH of the electrolyte}) + 0.198 \quad (1)$$

At pH 6.8, the flat band potentials on the RHE scale were calculated to be 2.48 V for BM, −0.28 V for UN, and 0.52 V for BR. For p-type semiconductors, the flat band potential is typically located 0.2 eV above the valence band maximum (VBM). Therefore, BM's valence band (VB) position was calculated to be 2.68 V *vs.* RHE. Its conduction band was evaluated to be 0.74 V (*vs.* RHE) by using eqn (2). The flat band potential for n-type semiconductors is approximately 0.2 eV below the conduction band minimum (CBM).[52] Accordingly, the CBMs for UN and BR were determined to be −0.48 V (*vs.* RHE) and 0.32 V (*vs.* RHE), respectively. Following eqn (2), the VBMs of UN and BR were estimated to be 1.99 V (*vs.* RHE) and 3.08 V (*vs.* RHE), respectively.

$$E_{CB} = E_{VB} - E_g \quad (2)$$

3.5 Evaluation of photocatalytic efficiency

The photocatalytic efficiency of the prepared catalysts was evaluated by the degradation of CR dye and H_2O_2 production.

3.5.1 Photocatalytic CR degradation. The reaction parameters, like the initial pH of the dye solution, its concentration, and the catalyst dose, play a crucial role during photocatalytic degradation. In order to obtain optimised parameters for maximum CR degradation efficiency, the influence of these parameters was studied first and is presented in the SI (S2). Furthermore, the reusability and structural stability of the BBUN-4 photocatalyst were examined, and the results of the cycling tests are detailed in Section S2.3 of the SI. In order to achieve maximum photodegradation efficiency, photocatalytic reactions were carried out under optimised conditions such as solution pH 7.0, CR concentration 50 ppm, and catalyst dose 0.5 g L^{-1}. As illustrated in Fig. S2(e), BBUN-4 exhibited the highest photocatalytic efficiency of 97.25%, which is about 1.5 and 1.69 times higher than that of pristine BM and UN, respectively. To further explore the CR degradation ability of BBUN-4, photocatalytic reaction kinetics were conducted, and the CR removal rate for BM, UN, and BBUN-4 was determined using the Langmuir–Hinshelwood model, as shown in eqn (3).[53] The results displayed in Fig. 8(a) revealed that the photodegradation of CR followed pseudo-first-order kinetics. The determined rate constant values are presented in Fig. 8(b), from which it was evident that BBUN-4 exhibited the highest rate constant value of 0.05514 min^{-1}, which was about 2.9 and 3.4 times greater than that of pristine UN and BM, respectively. The photocatalytic removal of CR was also carried out by using the fabricated heterostructures, namely BBUN-1, BBUN-2, BBUN-3, and BBUN-5. As observed from Fig. S2(f), the photodegradation efficiency of the heterostructures was increased up to BBUN-4 with the rise in BM quantity. However, the degradation percentage decreased to 90.1% when the BM content reached its highest level in BBUN-5. The observed reduction in efficiency can be ascribed to excessive semiconductor loading, leading to agglomeration and a consequent reduction in active surface area available for photocatalytic reactions.[54] The exceptional performance of BBUN-4 in CR removal may be attributed to the enormous surface area, wider range of light absorption in the visible region, abundantly available photoinduced excitons, minimal rate of electron–hole pair recombination, and faster charge carrier transfer across the interface.

$$\ln\left(\frac{C}{C_0}\right) = -kt \quad (3)$$

where C and C_0 indicate CR's concentration at time t, and its initial concentration, respectively, and k is the rate constant.

3.5.2 Photocatalytic H_2O_2 production performance. The photocatalytic performance of BM, UN, and BBUN-4 was again evaluated by H_2O_2 production under visible light illumination. As expected, BBUN-4 exhibited the highest H_2O_2 production efficiency in comparison to the other two pristine samples. The H_2O_2 yield displayed in Fig. 8(c) was found to be 127, 164, and 322 μmol L^{-1} for BM, UN, and BBUN-4, respectively. The highest H_2O_2 yield shown by BBUN-4 may be ascribed to its superior O_2 activation ability, which, in turn, is due to the preservation of photoinduced electrons with adequate thermodynamic propensity. A comparative analysis of H_2O_2 production efficiency between BBUN-4 and various reported catalysts is summarized in Table 1.[55–59]

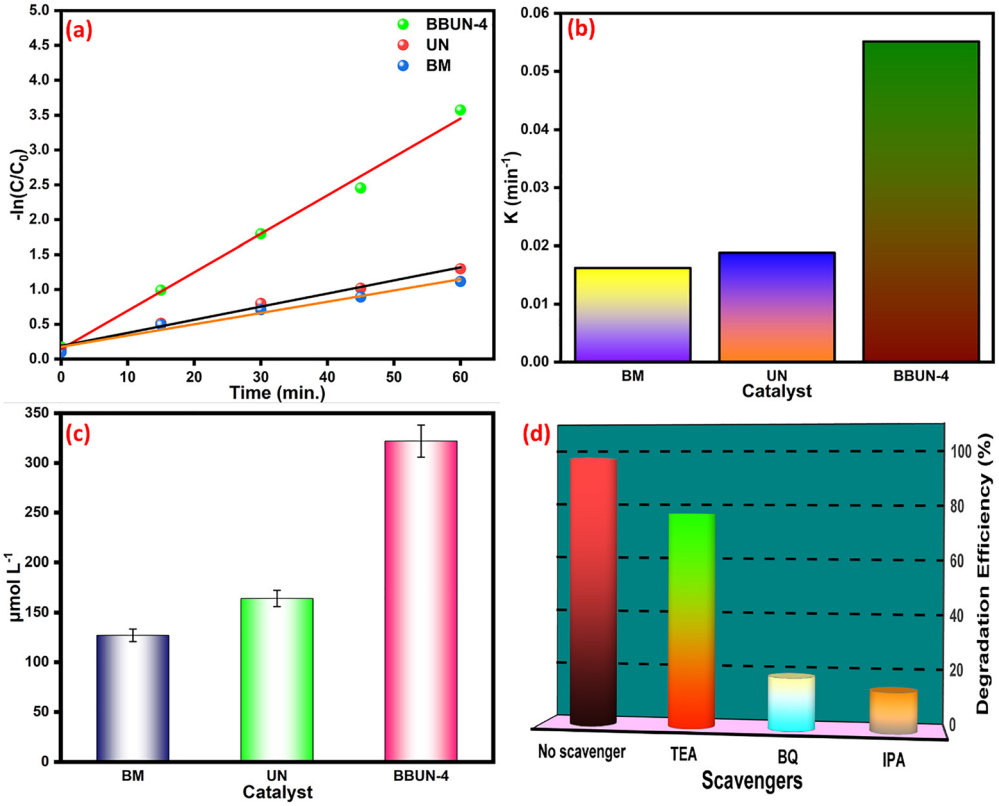

Fig. 8 (a) Reaction kinetics, (b) rate constant, and (c) H_2O_2 yield of BM, UN, and BBUN-4, and (d) scavengers experiment results.

Table 1 Comparison of photocatalytic H_2O_2 production by various catalysts with BBUN-4

Catalyst	Light	H_2O_2 yield	Ref.
Bi/Bi_2O_3@g-C_3N_4	Vis	92.51 µmol L^{-1}	55
Cu@Au/$BiVO_4$	Vis	91.1 µmol L^{-1}	56
CN/CNF_P	Vis	130.7 µmol L^{-1}	57
ZNO nanorods	Vis	285 µmol L^{-1}	58
$ZnIn_2S_4$/DUiO-66-NH_2	Vis	340 µmol L^{-1}	59
UiO-66-NH_2/BiOI@α-Bi_2O_3	Vis	322 µmol L^{-1}	This study

3.6 Photocatalytic reaction mechanism

Appropriate hybridisation of BM microspheres, *in situ* synthesised BR nanorods, and UN nanoparticles made BBUN-4 possess an extremely large surface area, porous architectures, enormous O_v at the interface, and an O_v–Bi–N interfacial charge transfer channel. As a result, it exhibited a wide range of visible light absorption windows, enriched photo-induced charge carriers, and a fast charge transfer rate, which cumulatively led to amplified photoactivity towards CR degradation and H_2O_2 production. To further understand the boosted pursuit of the ternary heterojunction, plausible charge transfer dynamics were elucidated. Usually, h^+, $^\bullet OH$, and $^\bullet O_2^-$ are considered the crucial reactive species for the photodegradation of organic compounds. In order to explore the primary reactive species involved in the degradation of CR, radical trapping experiments were carried out. Triethanolamine (TEA), isopropyl alcohol (IPA), and 1,4-benzoquinone (BQ) were used as the quenching agents for h^+, $^\bullet OH$, and $^\bullet O_2^-$, respectively.[60] The CR degradation efficiency of BBUN-4 in the presence of different scavenging agents is presented in Fig. 8(d). It was observed that 97.25% of CR was degraded in the absence of any trapping agent. However, the degradation efficiency sharply declined to 18.7% and 14.3% in the presence of BQ and IPA, respectively. Upon the addition of TEA, the degradation percentage was found to be 76.2%. These results suggested that both $^\bullet O_2^-$ and $^\bullet OH$ are the dominant reactive species driving the photocatalytic CR degradation, while h^+ plays a minor role.

The formation of $^\bullet O_2^-$ and $^\bullet OH$ can be ascertained if the thermodynamic criteria need to be satisfied by the heterostructured photocatalysts. The thermodynamic requirement for the release of $^\bullet O_2^-$ is that the conduction band edge level (E_{CB}) of the semiconductor photocatalyst must be more anodic than the standard reduction potential of the oxygen reduction reaction ($E^0_{O_2/^\bullet O_2} = -0.33$ eV *vs.* RHE, pH = 7.0). Similarly, the valence band edge position (E_{VB}) should be placed below the standard redox potential of the water oxidation reaction ($E^0_{H_2O/^\bullet OH} = 2.28$ eV *vs.* RHE, pH = 7.0) in order to meet the thermodynamic feasibility for the production of $^\bullet OH$ radicals. Therefore, the CB edge and VB levels of UN, BM, and BR were determined by the Mulliken electronegativity formula presented in eqn (4).

$$E_{VB} = X - E_e + 0.5E_g \quad (4)$$

where E_g is the band gap energy of the photocatalyst, E_e is the energy of free electrons on the hydrogen scale (4.5 eV), and X

represents the absolute electronegativity of the semiconductor. The E_g values for UN and BM were determined from UV-Vis DRS analysis as 2.47 eV and 1.94 eV, respectively, whereas that of BR was reported as 2.76 eV. The values of X for UN, BR, and BM were found to be 5.25, 6.03, and 6.21 eV, correspondingly. Putting these values in eqn (4), the E_{VB} values of UN, BM, and BR were calculated to be 2.05 eV, 2.65 eV, and 2.96 eV, respectively. Accordingly, the E_{CB} values were determined to be −0.42 eV, 0.71 eV, and 0.2 eV for UN, BM, and BR, respectively, after putting the corresponding E_{VB} values in eqn (2). These results are consistent with those obtained by Mott–Schottky (MS) analysis.

To propose a plausible charge transfer mechanism in the ternary heterojunction for required reactive species production, the type II pathway was first considered. According to it, photogenerated electrons can migrate from the CB of UN with a more negative energy level to that of BM and BR with a less negative potential. Simultaneously, holes are transferred from a more positive VB level of BM and BR to that with a less positive position of UN, as shown in Scheme 2. The CB potentials of BM (0.74 eV) and BR (0.32 eV) are placed below the potential required for the oxygen reduction reaction (ORR). Therefore, the electrons accumulated on the CB of BM and BR possessed inadequate reduction ability to generate $^{\bullet}O_2^-$. On the other hand, the holes (h^+) accumulated on the VB of UN cannot produce $^{\bullet}OH$ free radicals as the VB potential is less cathodic than that required for the water oxidation reaction (WOR). However, these outcomes contradict the results obtained from quenching experiments. This suggests that the type II charge transfer mechanism cannot satisfy the thermodynamic requirements for the production of $^{\bullet}O_2^-$ and $^{\bullet}OH$ species. In order to validate the feasibility of $^{\bullet}O_2^-$ and $^{\bullet}OH$ formation during the photocatalytic reactions, a binary Z-scheme charge transfer dynamics was proposed. In this system, all three semiconductors, UN, BM, and BR, generate electron–hole pairs upon exposure to solar light. According to XPS analysis, UN functions as an electron acceptor while BR and BM serve as electron donors. The photoinduced electrons from the CB of BM and BR with weaker redox potentials are transported through O_v–Bi–N charge transfer channels to recombine with the holes present at the VB of UN, which has inadequate redox ability. As a result, the photogenerated electrons at the CB of UN and holes at the VB of BR and BM with strong redox abilities are preserved for the production of $^{\bullet}O_2^-$ and $^{\bullet}OH$ species. Therefore, considering the results of scavenging tests, XPS studies, and band structure analysis, it was corroborated that the photocatalytic CR degradation over BBUN-4 proceeds through the construction of a double Z-scheme heterojunction. Additionally, the appearance of $^{\bullet}O_2^-$ as a primary reactive species suggested that the activation of O_2 is facilitated by the introduction of O_v, followed by reduction using the photogenerated electrons with high redox potentials preserved at the CB of UN, resulting in the binary Z-scheme charge transfer dynamics. The generated $^{\bullet}O_2^-$ undergoes a reaction with H^+ ions to produce H_2O_2. Thus, the photocatalytic production of H_2O_2 by BBUN-4 is likely to proceed through a two-step-one-electron transfer mechanism.[61] Initially, oxygen (O_2) molecules adsorbed on the BBUN-4 surface are reduced by available photoproduced electrons to form superoxide radicals ($^{\bullet}O_2^-$), which are further reduced to release H_2O_2 as per eqn (5).[62]

$$^{\bullet}O_2^- + e^- + 2H^+ \rightarrow H_2O_2 \quad (5)$$

Following the preceding analysis, the possible mechanism for photocatalytic CR degradation and H_2O_2 production is presented in Scheme 3.

4. Conclusion

A series of UiO-66-NH_2/BiOI@α-Bi_2O_3 ternary heterojunction photocatalysts were fabricated through a solvothermal route.

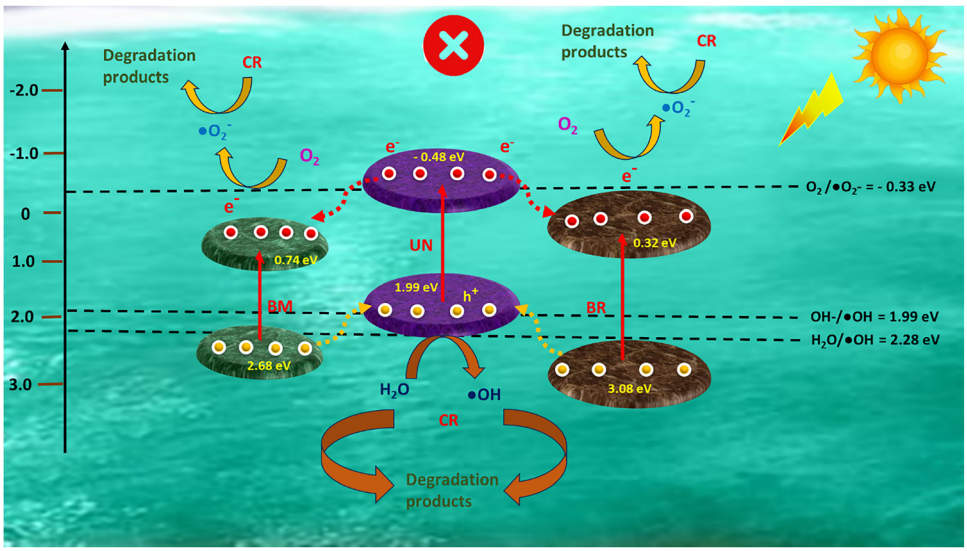

Scheme 2 Photocatalytic mechanism of BBUN-4 showing a type II charge transfer pathway for possible CR degradation and H_2O_2 production.

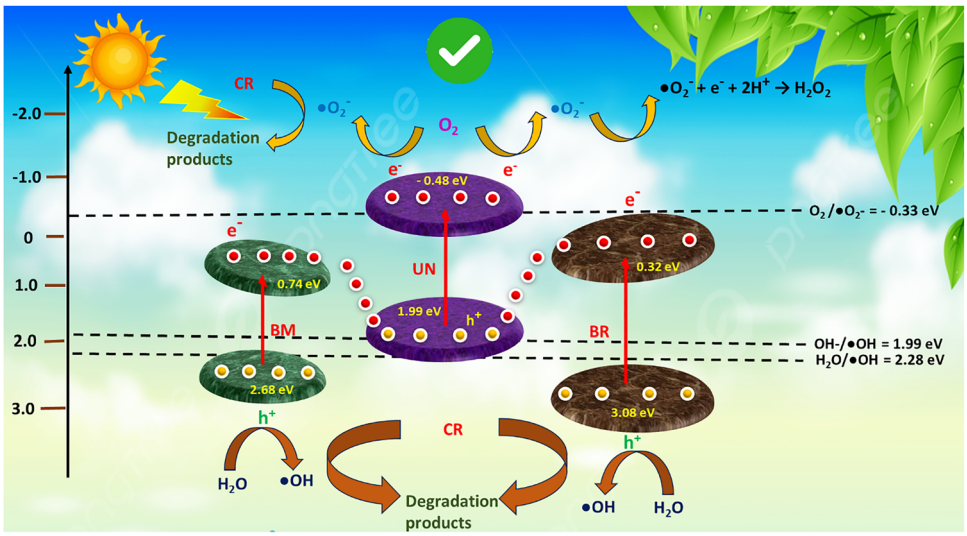

Scheme 3 Proposed binary Z-scheme charge transfer process for photocatalytic CR degradation and H_2O_2 production over BBUN-4.

By controlling the BM and DMF ratio, a ternary BBUN heterojunction with the desired morphology was obtained. When the BM : DMF ratio was maintained at 7.5 : 1, a BBUN-4 heterostructure was obtained with UN nanoparticles, BM microspheres, and *in situ* derived BR nanorods, which were revealed from FESEM and TEM studies. The formation of the ternary heterojunction containing these three components was also evident from UV-Vis DRS results. BBUN-4 possessed many advantageous features like enlarged surface area, mesoporous nature, and interconnecting porous architecture that were found beneficial for its superior photocatalytic performance over the pristine counterparts. The high surface area and mesoporous nature enable it for better dye and O_2 adsorption, whereas the interconnecting porous architecture assists in harvesting abundant visible light, which facilitates the enrichment of charge carriers. As revealed from HRTEM and XPS results, abundant O_v were introduced at the interfaces, resulting in a shift of the visible light absorption window to the red end and magnified O_2 activation. EIS analysis corroborated that BBUN-4 exhibited the smallest charge transfer resistance, indicating a faster charge transfer rate, which was supported by PL spectra showing reduced charge recombination. LSV confirmed the enhanced photocurrent responses for BBUN-4, further validating its superior charge separation and migration capabilities, attributed to the O_v–Bi–N interfacial charge transfer channel. The binary Z-scheme charge transfer dynamics preserved the photoexcitons with higher redox ability. Overall, BBUN-4 possessed high pollutant adsorption and O_2 activation capability, extended visible light absorption characteristics, maximum charge carrier concentration, minimal charge recombination rate, and robust redox ability. As a result, it exhibited an outstanding CR photodegradation efficiency of 97.25% at pH 7, in a 50-ppm solution and a 0.5 g L^{-1} catalyst dose, outperforming both BM and UN. The photocatalytic H_2O_2 production was also significantly enhanced by BBUN-4, with a yield of 322 μmol L^{-1}, far exceeding that of BM and UN. This study demonstrates the synergistic effect of the morphology-based ternary heterojunction, O_v–Bi–N interfacial charge transfer channel, and double Z-scheme charge transfer dynamics for efficient photodegradation of CR and H_2O_2 production.

Conflicts of interest

There are no conflicts to declare.

Data availability

The main article and the supplementary information (SI) include all the data generated or analyzed in this study. Supplementary information is available. See DOI: https://doi.org/10.1039/d5ma01197c.

Acknowledgements

The authors sincerely acknowledge the support and encouragement provided by the management of Siksha 'O' Anusandhan (Deemed to be University), Bhubaneswar, Odisha, India, which contributed significantly to the successful completion of this work.

References

1 M. Y. Qi, M. Conte, M. Anpo, Z. R. Tang and Y. J. Xu, Cooperative Coupling of Oxidative Organic Synthesis and Hydrogen Production over Semiconductor-Based Photocatalysts, *Chem. Rev.*, 2021, **121**(21), 13051–13085.
2 D. Gunawan, J. Zhang, Q. Li, C. Y. Toe, J. Scott, M. Antonietti, J. Guo and R. Amal, Materials Advances in Photocatalytic Solar Hydrogen Production: Integrating Systems and Economics for a Sustainable Future, *Adv. Mater.*, 2024, **36**(42), 2404618.
3 S. Mansingh, S. Sultana, R. Acharya, M. K. Ghosh and K. M. Parida, Efficient Photon Conversion via Double Charge

Dynamics CeO_2-$BiFeO_3$ p-n Heterojunction Photocatalyst Promising toward N_2 Fixation and Phenol-Cr(VI) Detoxification, *Inorg. Chem.*, 2020, **59**(6), 3856–3873.

4 Q. Wang and D. Astruc, State of the Art and Prospects in Metal-Organic Framework (MOF)-Based and MOF-Derived Nanocatalysis, *Chem. Rev.*, 2020, **120**(2), 1438–1511.

5 A. Jamma, B. Jaksani, C. S. Vennapoosa, S. Gonuguntla, S. Sk, M. Ahmadipour, M. Abraham B, I. Mondal and U. Pal, Defect-rich UiO-66@g-C_3N_4/Ni frameworks as efficient water splitting photocatalysts, *Mater. Adv.*, 2024, **5**, 2785–2796.

6 J. Liu, X. Sun, B. Jiang, M. Liu, Q. Li, X. Xiao, H. Wang, M. Zheng, S. Guo, J. Wu, Y. Zhang, K. Shi and W. Zhou, UiO-66-NH_2 Octahedral Nanocrystals Decorated with $ZnFe_2O_4$ Nanoparticles for Photocatalytic Alcohol Oxidation, *ACS Appl. Nano Mater.*, 2022, **5**, 2231–2240.

7 L. Jiang, D. Chen, Z. Hao, D. Cao, R. Liu, J. Cheng, L. Chen, X. Liu, B. Jia and D. Liu, An innovative Cu_xAg_{50-x}/UiO66-NH_2 photocatalyst prepared using a dual ship bottling strategy for photocatalytic CO_2 reduction: controlled product selectivity and pathways, *Energy Environ. Sci.*, 2024, **17**(21), 8228–8242.

8 Z. Jia, R. Li, P. Ji, Z. Xu, K. P. Homewood, X. Xia, Y. Gao, J. P. Zou and X. Chen, Design and fabrication of a novel 2D/3D $ZnIn_2S_4$@Ni/UiO-66-NH_2 heterojunction for highly efficient visible-light photocatalytic H_2 evolution coupled with benzyl alcohol valorization, *Appl. Catal., B*, 2024, **357**, 124279.

9 A. Mehtab and T. Ahmad, Unveiling the Bifunctional Photo/Electrocatalytic Activity of In Situ Grown CdSe QDs on g-C_3N_4 Nanosheet Z-Scheme Heterostructures for Efficient Hydrogen Generation, *ACS Catal.*, 2024, **14**(2), 691–702.

10 S. Zhang, J. Guo, S. Deng, R. Zhang, Q. Zhu, Y. Liu, X. Lin and Y. Li, Multifunctional BiOBr/BiOI 3D microspheres for improving visible-light-driven photocatalytic degradation and disinfection efficiency, *J. Environ. Chem. Eng.*, 2024, **12**(3), 113017.

11 R. Ji, Z. Zhang, L. Tian, L. Jin, Q. Xu and J. Lu, Z- scheme heterojunction of BiOI nanosheets grown in situ on NH_2-UiO-66 crystals with rapid degradation of BPA in real water, *Chem. Eng. J.*, 2023, **453**, 139897.

12 X. Li, H. Sun, Y. Xie, Y. Liang, X. Gong, P. Qin, L. Jiang, J. Guo, C. Liu and Z. Wu, Principles, synthesis and applications of dual Z-scheme photocatalysts, *Coord. Chem. Rev.*, 2022, **467**, 214596.

13 M. Kempasiddaiah, R. Samanta, R. K. Trivedi, D. Shrivastava, B. Chakraborty and S. Barman, Single-Crystalline α-Bi_2O_3 Induced by Nitrogen Doping for Enhanced and Selective CO_2 Electroreduction to Formate over a Wide Negative Potential Window, *ACS Appl. Energy Mater.*, 2024, **7**, 8465–8477.

14 Q. Yan, X. Xie, Y. Liu, S. Wang, M. Zhang, Y. Chen and Y. Si, Constructing a new Z-scheme multi-heterojunction photocataslyts Ag-AgI/BiOI-Bi_2O_3 with enhanced photocatalytic activity, *J. Hazard. Mater.*, 2019, **371**, 304–315.

15 Y. C. Liang, Y. H. Chou, B. Y. Chen and W. Y. Sun, Controllable Crystal Growth and Improved Photocatalytic Activity of Porous Bi_2O_3-Bi_2S_3 Composite Sheets, *ACS Omega*, 2023, **8**(29), 26055–26064.

16 T. Zhang, Y. Wang, X. Xie, Y. Shao, Y. Zeng, S. Zhang, Q. Yan and Z. Li, Dual Z-scheme 2D/3D carbon-bridging modified g-C_3N_4/BiOI-Bi_2O_3 composite photocatalysts for effective boosting visible-light-driven photocatalytic performance, *Sep. Purif. Technol.*, 2021, **277**, 119443.

17 R. R. Wary, M. Narzary, S. K. Nikhil, R. G. Nair, P. Kalita and M. B. Baruah, Rational construction of carbon-rich g-C_3N_4 wrapped over $CePO_4$ nanorods: Oxygen vacancy mediated 1D/2D Z-scheme photocatalyst towards removal of congo red dye, *Colloids Surf., A*, 2024, **684**, 133142.

18 D. Lu, J. Fan, X. Ma, M. Geng, J. Li and T. Xu, Dual-Functional Passivation Agent of Natural Dye Congo Red For Enhanced Carbon-Based Perovskite Solar Cells, *ACS Appl. Mater. Interfaces*, 2024, **16**, 69439–69449.

19 L. Acharya, G. Swain, B. P. Mishra, R. Acharya and K. Parida, Development of $MgIn_2S_4$ Microflower-Embedded Exfoliated B-Doped g-C_3N_4 Nanosheets: p-n Heterojunction Photocatalysts toward Photocatalytic Water Reduction and H_2O_2 Production under Visible-Light Irradiation, *ACS Appl. Energy Mater.*, 2022, **5**(3), 2838–2852.

20 Y. Hu, Z. Yang, D. Zheng, W. Xing and G. Zhang, Rational synthesis of carbon-rich hollow carbon nitride spheres for photocatalytic H_2O_2 production and Cr(VI) reduction, *Nanoscale*, 2025, **17**(13), 7856–7864.

21 J. Song, J. M. Yu, J. H. Ahn, H. Cho, J. Oh, Y. S. Kim, J. Kim, M. Ko, S. H. Lee, T. J. Shin, H. Y. Jeong, C. Yang, J. H. Lee, J. W. Jang and S. Cho, Selective, Stable, Bias-Free, and Efficient Solar Hydrogen Peroxide Production on Inorganic Layered Materials, *Adv. Funct. Mater.*, 2022, **32**(25), 2110412.

22 S. Mishra, L. Acharya, B. Marandi, K. Sanjay and R. Acharya, Boosted photocatalytic accomplishment of 3D/2D hierarchical structured Bi4O_5I_2/g-C_3N_4 p-n type direct Z-scheme heterojunction towards synchronous elimination of Cr(VI) and tetracycline, *Diamond Relat. Mater.*, 2024, **142**, 110834.

23 N. Khosroshahi, M. D. Goudarzi, M. E. Gilvan and V. Safarifard, Collocation of $MnFe_2O_4$ and UiO-66-NH_2: An efficient and reusable nanocatalyst for achieving high-performance in hexavalent chromium reduction, *J. Mol. Struct.*, 2022, **1263**, 132994.

24 X. Wang, J. You, Y. Xue, J. Ren, K. Zhang, B. Fu, Q. Xue, J. Tian and H. Zhang, Structural regulation of three-dimensional bismuth vanadate nanochannels for excellent visible light photocatalytic nitrogen fixation, *Appl. Catal., B*, 2025, **363**, 124817.

25 L. Chen, C. Li, Y. Zhao, J. Wu, X. Li, Z. Qiao, P. He, X. Qi, Z. Liu and G. Wei, Constructing 3D Bi/$Bi_4O_5I_2$ microspheres with rich oxygen vacancies by one-pot solvothermal method for enhancing photocatalytic activity on mercury removal, *Chem. Eng. J.*, 2021, **425**, 131599.

26 D. He, C. Wang, R. Zhao, X. Lu, M. Yang, J. Qiu, K. Wang and C. Wang, BiOX (X = Cl, Br, I)/WO_3/Polyacrylonitrile Nanofibrous Membranes for Diagnostic X-Ray Shielding and Visible-Light Photocatalysis, *ACS Appl. Nano Mater.*, 2022, **5**(3), 4157–4169.

27 S. Padhiari and G. Hota, A Ag nanoparticle functionalized Sg-C_3N_4/Bi_2O_3 2D nanohybrid: a promising visible light

harnessing photocatalyst towards degradation of rhodamine B and tetracycline, *Nanoscale Adv.*, 2019, **1**, 3212.

28 S. K. Nayak, S. K. Pradhan, S. Panda, R. Bariki and B. G. Mishra, MOF derived hierarchical α-Bi_2O_3-$BiVO_4$-$CuFe_2O_4$ multijunction heterostructure with conjugated S-scheme charge mobilization: Photocatalytic decontamination study, toxicity assessment and mechanistic elucidation, *Appl. Catal., B*, 2025, **360**, 124534.

29 H. Daneshgar, S. Sojdeh, G. Salehi, M. Edrisi, M. Bagherzadeh and N. Rabiee, Comparative study of synthesis methods and pH-dependent adsorption of methylene blue dye on UiO-66 and NH_2-UiO-66, *Chemosphere*, 2024, **353**, 141543.

30 Z. Yang, J. Cao, Y. Chen, X. Li, W. Xiong, Y. Zhou, C. Zhou, R. Xu and Y. Zhang, Mn-doped zirconium metal-organic framework as an effective adsorbent for removal of tetracycline and Cr(VI) from aqueous solution, *Microporous Mesoporous Mater.*, 2019, **277**, 277–285.

31 S. Bose and M. Kumar, Comparative evaluation of α-Bi_2O_3/$CoFe_2O_4$ and ZnO/$CoFe_2O_4$ heterojunction nanocomposites for microwave induced catalytic degradation of tetracycline, *Chemosphere*, 2024, **364**, 143071.

32 C. F. Holder and R. E. Schaak, Tutorial on Powder X-ray Diffraction for Characterizing Nanoscale Materials, *ACS Nano*, 2019, **13**(7), 7359–7365.

33 L. Yang, Z. Chen, G. Han, M. Hong, L. Huang and J. Zou, Te-Doped Cu_2Se nanoplates with a high average thermoelectric figure of merit, *J. Mater. Chem. A*, 2016, **4**, 9213.

34 K. Chakarova, I. Strauss, M. Mihaylov, N. Drenchev and K. Hadjiivanov, Evolution of acid and basic sites in UiO-66 and UiO-66-NH_2 metal-organic frameworks: FTIR study by probe molecules, *Microporous Mesoporous Mater.*, 2019, **281**, 110–122.

35 I. Ahmad, M. S. Athar, M. Muneer, H. M. Altass, R. F. Felemban and S. A. Ahmed, Graphene oxide decorated BiOI/CdS nanocomposite: An efficient ternary heterostructure for photodegradation and adsorption study of organic pollutants, *Surf. Interfaces*, 2024, **45**, 103819.

36 B. Yan, G. Chen, B. Ma, Y. Guo, Y. Zha, J. Li, S. Wang, J. Liu, B. Zhao and H. Xie, Construction of surface plasmonic Bi nanoparticles and α-Bi_2O_3 co-modified TiO_2 nanotube arrays for enhanced photocatalytic degradation of ciprofloxacin: Performance, DFT calculation and mechanism, *Sep. Purif. Technol.*, 2024, **330**, 125180.

37 P. J. Mafa, M. E. Malefane, F. Opoku, A. O. Oladipo, G. Mamba, T. L. Yusuf, J. F. Nure, S. L. Lebelo, D. Liu, J. Gui, B. B. Mamba and A. T. Kuvarega, Dual Charge Transfer Mechanisms in Intimately Bonded S-scheme Heterojunction Photocatalyst with Expeditious Activity toward Environmental Remediation, *Adv. Sustainable Syst.*, 2025, **9**, 2401070.

38 Z. Xia, L. Wang, W. Tan, L. Yuan, X. He, J. Wang, L. Chen, S. Zen, S. Lu and Z. Jiao, Visible-Light Photocatalytic Degradation Efficiency of Tetracycline and Rhodamine B Using a Double Z-Scheme Heterojunction Catalyst of UiO-66-NH_2/BiOCl/Bi_2S_3, *Inorg. Chem.*, 2024, **63**(31), 14578–14590.

39 R. Bariki, S. K. Pradhan, S. Panda, S. K. Nayak, A. R. Pati and B. G. Mishra, Hierarchical UiO-66(–NH_2)/$CuInS_2$ S-Scheme Photocatalyst with Controlled Topology for Enhanced Photocatalytic N_2 Fixation and H_2O_2 Production, *Langmuir*, 2023, **39**, 7707–7722.

40 T. V. L. Thejaswini, D. Prabhakaran and M. A. Maheswari, Soft synthesis of Bi Doped and Bi-N co-doped TiO_2 nanocomposites: A comprehensive mechanistic approach towards visible light induced ultra-fast photocatalytic degradation of fabric dye pollutant, *J. Environ. Chem. Eng.*, 2016, **4**(1), 1308–1321.

41 Q. Meng, A. Kravchenko, B. Zhang, H. Yang, C. Liu, Y. Li, X. Sheng, L. Fan, F. Li and L. Sun, Remarkable synergy of borate and interfacial hole transporter on BiVO4 photoanodes for photoelectrochemical water oxidation, *Mater. Adv.*, 2021, **2**, 4323.

42 Q. Wang, H. Wu, Q. Gao, D. Lin, Y. Fan, R. Duan, Y. Cong and Y. Zhang, Fabrication of visible-light-active Bi/BiOI-Bi_2O_3 composite with enhanced photocatalytic activity, *J. Colloid Interface Sci.*, 2019, **548**, 255–264.

43 X. Cheng, X. Xiao, F. Wang, T. Lu and Y. Zhang, Heterojunctions Based on BiOBr Nanosheets Decorated on α-Bi_2O_3 for Photodegradation of Rhodamine B, *ACS Appl. Nano Mater.*, 2024, **7**, 4413–4422.

44 S. Mishra, B. L. Tudu, N. Mishra, K. Sanjay and R. Acharya, Fabrication of oxygen vacancy modified 2D–2D g-C_3N_4/$ZnFe_2O_4$ heterostructures for amplifying photocatalytic methyl orange degradation and hydrogen production, *Mater. Adv.*, 2025, **6**, 9085.

45 L. Hao, H. Huang, Y. Zhang and T. Ma, Oxygen Vacant Semiconductor Photocatalysts, *Adv. Funct. Mater.*, 2021, **31**(25), 2100919.

46 D. Cui, L. Wang, K. Xu, L. Ren, L. Wang, Y. Yu, Y. Du and W. Hao, Band-gap engineering of BiOCl with oxygen vacancies for efficient photooxidation properties under visible-light irradiation, *J. Mater. Chem. A*, 2018, **6**, 2193–2199.

47 X. Cheng, X. Xiao, F. Wang, T. Lu and Y. H. Zhang, Heterojunctions Based on BiOBr Nanosheets Decorated on α-Bi2O3 for Photodegradation of Rhodamine B, *ACS Appl. Nano Mater.*, 2024, **7**, 4413–4422.

48 H. Li, J. Shi, K. Zhao and L. Zhang, Sustainable molecular oxygen activation with oxygen vacancies on the {001} facets of BiOCl nanosheets under solar light, *Nanoscale*, 2014, **6**, 14168.

49 K. A. Tsai, J. C. Chang and Y. C. Pu, Charge Carrier Dynamics at Heterojunction of Semiconductor Nanoheterostructures for Photocatalytic Solar Fuel Generation, *Adv. Energy Sustainability Res.*, 2025, 2400329.

50 D. Ping, F. Yi, G. Zhang, S. Wu, S. Fang, K. Hu, B. Bin Xu, J. Ren and Z. Guo, NH_4Cl-assisted preparation of single Ni sites anchored carbon nanosheet catalysts for highly efficient carbon dioxide electroreduction, *J. Mater. Sci. Technol.*, 2023, **142**, 1–9.

51 X. Xiao, S. Li, L. Zuo, R. Li, Z. Li, L. Liu, H. Fan and B. Li, Twin S-Scheme Heterojunction ZnO/UiO-66-NH_2@$ZnIn_2S_4$ Rhombic Octahedra for Efficient Photocatalytic H_2 Evolution, *Adv. Funct. Mater.*, 2025, 2418778.

52 S. Mishra, L. Acharya, S. Sharmila, K. Sanjay and R. Acharya, Designing g-C_3N_4/$NiFe_2O_4$ S-scheme heterojunctions for

efficient photocatalytic degradation of Rhodamine B and tetracycline hydrochloride, *Appl. Surf. Sci. Adv.*, 2024, **24**, 100647.

53 S. Mishra and R. Acharya, Recent updates in modification strategies for escalated performance of Graphene/MFe_2O_4 heterostructured photocatalysts towards energy and environmental applications, *J. Alloys Compd.*, 2023, **960**, 170576.

54 Y. Tang, J. Qiu, D. Dai, G. Xia, B. Fang, Y. Li and J. Yao, $ZnIn_2S_4$/MIL-53-NH_2 composite photocatalysts for H_2O_2 production: Synergistic effect of sulfur vacancy and heterostructure, *Sep. Purif. Technol.*, 2025, **354**, 129350.

55 X. Yan, G. Yu, C. Xing, Y. Hu, H. Liu and X. Li, Schottky junction with Bi/Bi2O3 core–shell nanoparticle modified g-C3N4 for boosting photocatalytic H2O2 evolution from pure water, *Catal. Sci. Technol.*, 2023, **13**, 3094.

56 T. Shan, Y. Wang, D. Luo, Z. Huang, F. Zhang, H. Wu, L. Huang, J. Li, L. Chen and H. Xiao, Extended H-bonds/π-bonds networks for boosting electron transfer over polydopamine-covered nanocellulose/g-C_3N_4 toward efficient photocatalytic H_2O_2 production, *Appl. Catal., B*, 2024, **349**, 123872.

57 Z. Jiang, Y. Zhang, L. Zhang, B. Cheng and L. Wang, Effect of calcination temperatures on photocatalytic H_2O_2-production activity of ZnO nanorods, *Chin. J. Catal.*, 2022, **43**(2), 226–233.

58 Y. Tang, J. Qiu, D. Dai, G. Xia, L. Zhang and J. Yao, Defect-engineered Zr-MOFs with enhanced O_2 adsorption and activation for photocatalytic H_2O_2 synthesis, *Catal. Sci. Technol.*, 2024, **14**(1), 83–89.

59 A. Mondal, A. Prabhakaran, S. Gupta and V. R. Subramanian, Boosting Photocatalytic Activity Using Reduced Graphene Oxide (RGO)/Semiconductor Nanocomposites: Issues and Future Scope, *ACS Omega*, 2021, **6**, 8734–8743.

60 T. S. Prakash, S. Subudhi, S. Das, M. K. Ghosh, M. Das, R. Acharya, R. Acharya and K. Parida, Hydrolytically stable citrate capped Fe_3O_4@UiO-66-NH_2 MOF: A hetero-structure composite with enhanced activity towards Cr (VI) adsorption and photocatalytic H_2 evolution, *J. Colloid Interface Sci.*, 2022, **606**, 353–366.

61 A. Wang, H. Liang, F. Chen, X. Tian, S. Yin, S. Jing and P. Tsiakaras, Facile synthesis of C_3N_4/$NiIn_2S_4$ heterostructure with novel solar steam evaporation efficiency and photocatalytic H_2O_2 production performance, *Appl. Catal., B*, 2022, **310**, 121336.

62 S. Jing, J. Zhao, A. Wang, Q. Ji, R. Cheng, H. Liang, F. Chen, P. Kannan, A. Brouzgou and P. Tsiakaras, Efficient photocatalytic production of H_2O_2 and photodegradation of tetracycline by CdS/square tubular g-C_3N_4 S-scheme heterojunction photocatalyst, *Chem. Eng. J.*, 2024, **479**, 147150.